

# A text-based, generative deep learning model for soil reflectance spectrum simulation in the VIS-NIR (400-2499 nm) bands

Tong Lei<sup>1\*</sup> and Brian N. Bailey<sup>1</sup>

<sup>1</sup>Department of Plant Sciences, University of California, Davis, CA, USA

\*tlei@ucdavis.edu

## Abstract

Soil spectral reflectance is a necessary input for land surface and radiative transfer models, and can be used to infer soil properties. Numerous models have been developed based on mechanistic approaches, each with their own limitations. Mechanistic models based on radiative transfer theory are usually based on only a few input soil properties, whereas data-drive approaches are limited by high non-uniformity of available published datasets that severely limits the amount of data usable for model calibration. To address these limitations, a fully data-driven soil optics generative model (SOGM) for simulation of soil reflectance spectra based on soil property inputs was developed based on the denoising diffusion probabilistic model (DDPM). The model was trained on an extensive dataset comprising nearly 180,000 soil spectra-property set pairs from 17 published datasets. The model generates soil reflectance spectra from text-based inputs describing soil properties and their values rather than only numerical values and labels in binary vector format, which means the model can handle variable formats for property reporting. Because the model is generative, it can simulate reasonable output spectra based on an incomplete set of available input properties, which becomes more constrained as the input property set becomes more complete. Two additional sub-models were also built to complement the SOGM: a spectral padding model that can fill in the gaps for spectra shorter than the full visible-near-infrared range (VIS-NIR; 400 to 2499 nm), and a wet soil spectra model that can estimate the effects of water content on soil reflectance spectra given the dry spectrum predicted by the SOGM. The SOGM was up-scaled by coupling with the Helios 3D plant modeling software, which allowed for generation of synthetic aerial images of simulated soil and plant scenes. It can also be easily integrated with other soil-plant radiation models used for remote sensing research such as PROSAIL. The testing results of the SOGM on new datasets that not included in model training demonstrated that the model can generate reasonable soil reflectance spectra based on available property inputs. Results also show soil clay/sand/silt fraction, organic carbon content, nitrogen content, and iron content tended to be important properties for spectra simulation. Inclusion of some trace minerals like nickel as model inputs decreased model performance because of their low concentrations and large

propensity for ground-truth measurement error. The presented models are openly accessible on:  
[https://github.com/GEMINI-Breeding/SOGM\\_soil\\_spectra\\_simulation](https://github.com/GEMINI-Breeding/SOGM_soil_spectra_simulation).

## 1 Introduction

The spectral reflectance of soil determines how radiation of varying wavelength interacts with soil constituents, and thus indirectly contains information about the state and composition of the soil. It is therefore commonly used as a remotely measurable quantity for inferring information about the soil [1, 2], or as an input for models seeking to predict how radiation interacts with the soil surface. Land surface models are widely used to predict fluxes of energy, mass, and momentum at Earth’s surface, usually across large scales, and require soil reflectance spectra as an input to predict surface radiative energy exchange. Examples include 4SAIL2 [3], PROSAIL [4], soil-canopy observation photosynthesis and energy fluxes (SCOPE) model [5], and soil-plant-atmosphere radiative transfer (SPART) model for satellite measurements [6]. In other applications, soil reflectance spectra may be needed as an input for algorithms that use radiative transfer model inversion or machine learning models to determine physical properties of overlying vegetative canopies from remotely sensed images that contain both plant elements and background soil [7, 8, 9].

Because of the scale at which land surface models are often applied (i.e., regional to global), it is not feasible to manually measure the spatial variability in soil reflectance spectra, and thus it must be modeled. Soil reflectance spectra is commonly predicted using soil radiative transfer models that describe the relationship between soil reflectance and soil properties [1, 10, 11, 12, 13, 14]. The soil reflectance spectra depends on complex relationships between soil structure, aggregate constituents, and water content [15], and thus some input parameters for these models can be difficult to measure at scale, such as the absorption coefficient of soil [14, 15] or parameters fitted from customized empirical functions [10, 11]. As a result, these models typically rely on empirical relationships obtained from laboratory samples, and may thus have issues when applied at the field scale. Furthermore, previous soil radiative transfer models have primarily focused on a limited number of factors, such as moisture, organic matter, and particle size [1, 10, 11, 12, 13, 14]. However, many important soil properties like organic carbon, total nitrogen, and pH values, which also impact soil reflectance spectra, have not been integrated into most previous radiative transfer models for spectral simulation.

The extensive advancement in techniques for soil monitoring has motivated the curation of vast amounts of soil spectra and property ground truth data by various laboratories and institutes around the world [16, 17, 18, 19]. Given the limitations of semi-empirical radiative models for soil spectral simulation, a potential alternative is to use a fully data-driven approach that has the ability to incorporate large amounts of existing soil spectra-property datasets. However, the diversity and inconsistency of existing datasets presents additional challenges when using a data-driven approach. Spectra obtained from different instruments may have different measurement wavelengths, and may introduce biases into the data due to variability in the calibration or internal components of each instrument. In previous studies and datasets such as OSSL [19], one approach is to partially crop the data to fit to a wavelength range that is common across all datasets, but this discards a large

amount of potentially informative data. [20] developed a transformer-based predictive model that can handle soil spectra obtained by different instruments. However, for soil spectra simulation used in radiative transfer modeling [21, 4], where spectra that span the full visible to near-infrared wavelength range are normally required, it becomes necessary to generate the missing wavebands to ensure the completeness of the simulated data.

Another considerable challenge in using a data-driven approach for soil reflectance spectral modeling is that ground truth measurements of soil properties differ substantially across datasets, both in terms of which measurements were collected and how their values are reported. Soil properties are commonly incorporated into models as either quantitative values or qualitative labels [10, 1, 20]. However, some soil properties, like total phosphorus content and exchangeable phosphorus content, share complex relationships that are not easily captured using physical models. The same property may be described using different units, such as % or  $\text{g}/\text{dm}^3$ , making direct conversion between them impossible. Additionally, certain property values are represented as text-based labels, such as qualitative land use and land cover classifications, further complicating the integration of these properties into parameterized models. Therefore, directly inputting property values into a parameterized model can lead to several issues: it risks losing valuable connections among different soil properties; handling a combination of labels and numerical values within the same model becomes a challenging task; because different soil properties might be presented, relying solely on the sequence of values to identify specific properties within the model is likely to be an unreliable approach. Consequently, directly inputting text-based descriptions of soil properties into the model might be a better choice, as text descriptions inherently encode the property differences.

In this work, a soil optics generative model (SOGM) for simulation of soil reflectance spectra based on soil property inputs was developed. The modeling approach has three primary novel aspects that distinguish it from previous approaches. First, the model is fully data-driven and is trained on an extensive dataset comprising nearly 180,000 soil spectra and their measured physical properties. Second, it generates soil reflectance spectra from text-based inputs describing soil properties and their values rather than only numerical values and labels in binary vector format. Third, the model is generative, which means that it can simulate output spectra based on an incomplete set of input properties. In contrast to a predictive model which yields identical outputs for identical inputs, a generative model enables varied outputs for identical (incomplete) inputs. This is an important feature for soil optical modeling since many soil properties that can influence the soil reflectance spectra may not explicitly listed in available datasets used for model training, or the user may not know all soil properties when the model is applied for prediction. SOGM is based on the denoising diffusion model [22], which is popular in deep-learning-based image generation [23]. Two additional sub-models were created to complement the SOGM: a spectral padding model that can fill in the gaps for spectra shorter than the full visible-near-infrared range (VIS-NIR; 400 to 2499 nm), and a wet soil spectra model that can estimate the effects of water content on soil reflectance spectra given the dry spectrum predicted by the SOGM. The SOGM was up-scaled by coupling with the Helios 3D plant modeling software [24], which allowed for generation of synthetic aerial images of simulated soil and plant scenes.

## 2 Datasets and models

### 2.1 Datasets

In the current study, 17 dry soil VIS-NIR or NIR spectral datasets were utilized for training the spectra padding model and SOGM (Table 1). In certain datasets, such as OSSJ and LUCAS, spectra obtained from repeated scans on the same sample were retained to ensure a sufficiently large training set, resulting in a total of 177,579 soil spectra. The noisy segments and portions beyond the 400 to 2499 nm range of the spectra were manually excluded. For each spectrum, the first wavelength and the last wavelength, plus 1, that are not divisible by 50 were also omitted (the reason is given in Sect. 2.2). For example, if the first measured wavelength in the spectrum was 380 nm, it would be increased to 400 nm (wavelengths from 380-399 nm were removed), and for the last wavelength, 2360 nm would be trimmed to 2349 nm.

The final wavelength ranges for the datasets considered in this study are presented in Table 1. We believe this to be the largest compiled soil VIS-NIR spectra model to date. These datasets were acquired using spectrometers from various manufacturers, including FOSS NIRSystems Inc. (Hilleroed, Denmark), Analytical Spectral Devices (ASD) Inc., (Boulder, Colorado, USA), Bruker Optics (Ettlingen, Germany), Spectral Evolution, Inc. (Haverhill, Massachusetts, USA), Si-Ware Systems (Menlo Park, California, USA), and others. Instrument manufacturer was included as a variable in the model to account for potential biases due to instrument. While a single manufacturer like ASD offers different models such as the FieldSpec3, FieldSpec4, and LabSpec, the differences between versions from the same manufacturer are minor. Consequently, version information was omitted from the model to improve its generalizability (Table 3).

Table 2 lists three datasets used for testing the spectral padding and diffusion model, comprising a total of 652 dry soil spectra. The original MARMIT2020 data repository [10, 11] includes 8 sub-datasets [10, 11, 25, 26, 27, 28, 29] with a total of 1894 spectra, of which 211 are dry soil spectra. For all 3 datasets, outlier spectra were excluded, such as those with many values higher than 1 or with high noise level, and spectra with no valid properties. "Valid properties" refers to properties that appeared in the training datasets, including Clay, Silt, Sand, Soil organic matter,  $\text{CaCO}_3$ , Mg, Al, P, Ca, Mn, Fe, Zn, and Ni contents, pH value, Cation-exchange capacity, among others. Some property values were not provided in the original datasets, hence the average valid soil property values for some datasets are not integers in Table 2.

For the wet spectra model, both wet and dry spectra from the MARMIT2020 data repository [10, 11] and an additional 78 wet and dry spectra from [30] were used. More details are provided in Sect. 2.5.

### 2.2 Spectra padding model

The goal of the spectra padding sub-model is to standardize all spectra to a uniform wavelength interval spanning 400 to 2499 nm at 1 nm intervals, with consistent units. All raw spectral units were converted to wavelength, and spectral absorbance ( $\mathbf{A}$ ) values were converted to reflectance ( $\mathbf{R}$ )

Table 1: Datasets for model training

Datasets	Number of spectra	Selected wavelength range	Reference
LUCAS	62596	400-2499 nm	[16, 18]
ASSL	19323	400-2499 nm	[31]
BRC	1100	450-2499 nm	[32]
SER	108	400-2499 nm	[33]
OSSL	23847	400-2499 nm	[19]
UKC	105	400-2499 nm	[34]
BSSL	16094	400-2499 nm	[17, 35]
BASE	695	400-2499 nm	[36]
KEW	553	850-2499 nm	[37]
OSSLJ	48503	950-2499 nm	[38]
AFSIS	1907	850-2499 nm	[39]
BEL	83	400-2449 nm	[40]
BRT	102	450-2149 nm	[41]
FRT	1415	1000-2499 nm	[42, 43]
ITR	300	400-2499 nm	[44]
DAE	26	400-2499 nm	[45]
GER1	362	1350-2499 nm	[46]
GER2	362	400-2199 nm	[46]

Table 2: Datasets for model testing

Dataset	Number of samples	Valid soil property	Average number of soil property	Manufacturer of spectrometer	Reference
Barthès2023	404	Clay, Silt, Sand, Organic carbon, and Total nitrogen contents, Coarse fragment, and Bulk density	4.94	FOSS	[47]
Hu2020	47	Clay, Silt, Sand, Mg, Al, P, Ca, Mn, Fe, Zn, and Ni contents	10.47	Spectral Evolution	[48]
MARMIT2020	201	Clay, Silt, Sand, Soil organic matter, CaCO <sub>3</sub> , Organic carbon, and Total iron contents, Bulk density, pH value, and Cation-exchange capacity	4.96	ASD	[10, 11]

Table 3: Soil property examples

Property	Value example	Unit
Coarse fragments	1.0	%
Clay	1.0	%
Clay	1.0	$g/dm^3$
Silt	1.0	%
Sand	1.0	%
Cation exchange capacity	1.0	cmol(+)/kg
Cation exchange capacity	1.0	cmol(+)/ $dm^3$
pH measured from $CaCl_2$ solution	1.0	-
pH measured from water solution	1.0	-
Total carbon content	1.0	%
Organic carbon content	1.0	%
The primary land cover	Sunflower	-
The primary land use	Forestry	-
Exchangeable phosphorus content	1.0	mg/kg
Extractable phosphorus content	1.0	mg/kg
Total phosphorus content	1.0	mg/kg
Total potassium content	1.0	mg/kg
Total nitrogen content	1.0	g/kg
$CaCO_3$ content	1.0	g/kg
Percentage of stones in soil	<10	%
Country	United States	-
Province/State	California	-

according to the equation:  $\mathbf{R} = 1/10^A$ . If reflectance values were reported at an interval greater than 1 nm, linear interpolation was used to determine values at a 1 nm interval. The spectra were then organized into a matrix of size  $N \times 2100$ , where  $N$  is the total number of spectra in the dataset.

As described before, the soil spectral libraries obtained by different spectroscopic instruments may have different measurement wavelength ranges. If a spectrum had wavelengths ranging from 400 to 2499 nm, it will occupy the whole matrix row and no padding is needed. If its range is less than the maximum range, the missing values in the matrix row will initially be set to 0. Wavelengths exceeding the maximum range of 400 to 2499 nm are removed. An input spectrum with a shorter range will be expanded to span the entire 400 to 2499 nm using the spectra padding model.

The first embedding part of the spectra padding model is developed based on the encoder component of the soil spectra model of [20]. The vector of a spectrum was reshaped into a matrix with a shape of  $42 \times 50$ , where 42 is the number of wavebands, and 50 is the number of absorbance values in one waveband. In cases where the first or last waveband in the matrix is not fully filled, it is entirely set to zero. Consequently, the input spectral matrix was converted into a three-dimensional (3D) tensor (spectra tensor in Fig. 1).

Three transformer layers are then used to process this input data, designed so that the padding does not influence the calculations. In other words, the output of the model should be the same for tensors with any number of zero padding wavebands as long as the non-zero wavebands are the same. Therefore, a masked transformer was used to eliminate the effect of zero padding. The first two transformer layers use a self-attention mechanism, and if the input band is zero-padded, the

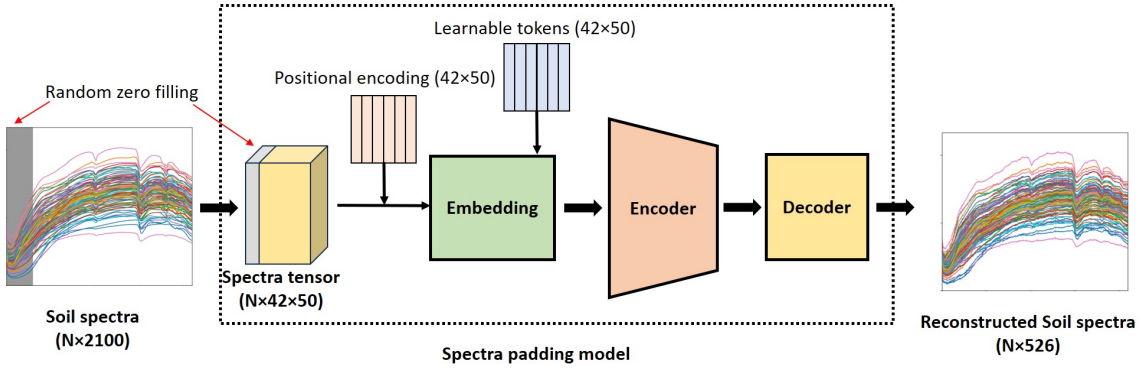


Figure 1: Schematic representation of the training and architecture of the spectra padding model. A portion of the input spectra is randomly set to 0 (indicated by the grey shadow), and the down-sampled, full-range input spectra are reconstructed. The embedding block consists of transformer layers, while the encoder and decoder blocks are composed of 1D CNN layers.

same index of the output will also be zero-padded. As the attention mechanism cannot recognize the order of input wavebands, positional encoding that adds position information of the tokens in the sequence is suggested [49, 20]. The positional encoding has the same dimension as the input spectra matrix so that the two can be summed. It should be noted that positional encoding is added only to non-zero bands. To make sure the outputs have the same shape without zero padding bands, the third transformer layer is based on a cross-attention mechanism. Specifically, 42 learnable tokens are used as query input of the third layer, and the output of the second layer is used as key and value input. Then, the output of spectral embedding enters an encoder and then a decoder. The encoder and decoder consist of one-dimensional (1D) convolution neural networks (CNN).

The input spectra undergo zero padding on randomly selected wavebands (Fig. 1). The target is the down-sampled input spectra without zero padding, still ranging from 400 to 2499 nm, but with a resolution of 4 nm, resulting in an output matrix of  $N \times 526$ . This down-sampling aims to accelerate model training and prevent overfitting.

The trained model is then capable of padding the missing wavelengths of input soil reflectance spectra. The output down-sampled spectra are up-sampled to align with the size of the input spectra ( $N \times 2100$ ) using linear interpolation. The non-padded parts of the up-sampled spectra are replaced with the original spectra. Lastly, a second-order Savitzky-Golay smoothing [50], with a window size of 100 nm, is applied to the padded parts of the spectra, resulting in the final full-wavelength spectra.

### 2.3 Property embedding

In the present study, we input text strings into the SOGM that include full soil property descriptions rather than just numerical values and labels. The properties from all the collected datasets were organised in the following format: “property: value unit”, with some examples shown in Table 3. This table reveals connections among various soil properties. Subsequently, a learnable word dictionary containing parameterized vectors was built. The total number of vectors corresponds

to the unique words present across all properties, meaning each vector represents a specific word. Consequently, a phrase like “Exchangeable phosphorus content: 1.0 mg/kg” can be converted into a matrix. Information about the spectrometer manufacturer is also input into the SOGM in the same format as other soil properties, for example, “Spectrometer manufacturer: ASD”. Numerical values in sentences are represented by the actual number along with a numerical value tag vector, and this tag is also included in the word dictionary.

Positional encodings are added to the sentence matrix to enable the model to identify the sequence of words. This matrix is then aggregated into a sentence embedding vector using transformer layers. These sentence embeddings are further combined to create a property embedding, employing additional transformer layers. However, positional encodings are not used for sentence embeddings, as soil properties do not possess an inherent order. The transformer layers produce consistent results regardless of the sentence embeddings’ order, provided the input sentence embeddings remain the same. All transformer layers in the property embedding model are equipped with masks, similar to those in Sect. 2.2, to accommodate varying sentence and word counts.

A predefined list, featuring text descriptions for 15 major soil properties, is provided alongside the codes. Users can consult the code for valid input values.

## 2.4 Denoising diffusion

The denoising diffusion probabilistic model (DDPM) proposed by [22] was developed for high-quality image generation, which is a class of latent variable models inspired from nonequilibrium thermodynamics. The diffusion process begins by gradually adding noise into a clear image over a series of time steps, effectively transforming the image into a noisy version. The specific time step indicates the stage within the diffusion process. Then, a U-Net model [51] is trained to predict the noise at each time step and subtract it from the noisy image. Through this iterative denoising, the model effectively ‘reverses’ the diffusion process. The key is that through learning to reverse this noise addition, the DDPM gradually reconstructs the original or a new image from the noisy state.

The text embeddings obtained by the property embedding model were integrated into the noise prediction by adding a transformer layer into the U-Net (Fig. 2). A 1D U-Net, which consists of 1D CNN layers, was employed due to the 1D nature of soil reflectance spectra data. For model training, random noise vectors were sampled and added to the spectra in different proportions as determined by the time step. The property text strings are input into the property embedding model to obtain the embeddings. Subsequently, the noisy spectra and corresponding property embeddings are fed into the U-Net model to predict the added noise. The property embedding model and the diffusion model are trained together to minimize the loss function  $\mathcal{L}$ , which is given by:

$$\mathcal{L} = \mathbb{E}_{t, \mathbf{R}_0, \epsilon} [\min(\text{SNR}(t), \lambda) \|\epsilon - \epsilon_{\theta}(\mathbf{R}_t, t)\|^2], \quad (1)$$

where  $\mathbb{E}$  is the expectation over the random variables,  $t$  denotes the time step in the diffusion process,  $\mathbf{R}_0$  is the original soil spectrum,  $\epsilon$  is the true noise added at time  $t$ ,  $\epsilon_{\theta}(\mathbf{x}_t, t)$  refers to the noise predicted by the model, given the noisy spectrum  $\mathbf{R}_t$  at time  $t$ ,  $\|\cdot\|^2$  denotes the squared Euclidean norm, used here to calculate the mean squared error, the factor  $\lambda$  is set to 5, and  $\text{SNR}(t)$



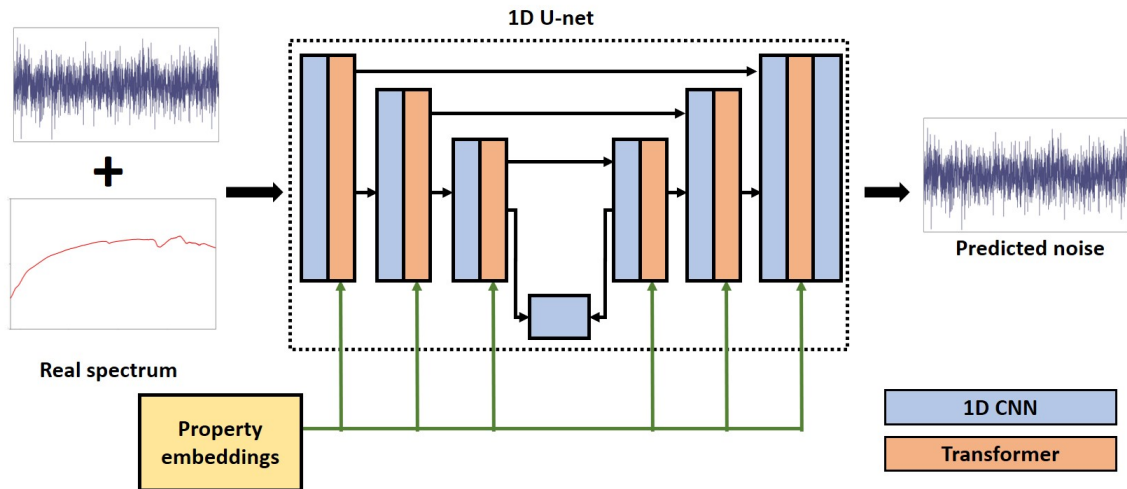


Figure 2: Schematic representation of the denoising diffusion model. The inputs consist of the sum of random noise and soil spectra, along with corresponding property  $s$ . The output is the input random noise during model training. The blue blocks represent 1D CNN layers, and the orange blocks represent transformer layers.

represents the signal-to-noise ratio at time  $t$ . It can be calculated by:  $\text{SNR}(t) = \frac{\bar{\alpha}_t}{1 - \bar{\alpha}_t}$ , where  $\bar{\alpha}_t$  is the product of noise scales  $\alpha$  from the start of the diffusion process up to time  $t$ . The use of  $\text{SNR}(t)$  is to avoid the model focusing too much on small noise levels [52].

Once trained, the model generates new spectra by reversing the diffusion process controlled by the target soil property text description. It starts with a sample of random noise and then iteratively applies the learned reverse transformations to reduce the noise. Each step in the reverse process involves applying the model to predict and subtract out the noise from the current spectrum, effectively denoising it (Fig. 3). The total number of time steps was set to 300, which was empirically found to consistently ensure adequate denoising efficiency and quality.

## 2.5 Wet soil spectra model

The gravimetric soil moisture content ( $SMC_g = \frac{100 \times (m_w - m_d)}{m_d}$ , where  $m_w$  and  $m_d$  are wet and dry soil weights for a given sample volume, respectively) is an external factor affecting the reflectance spectrum, but typically changes much more rapidly than other properties. Large soil spectral libraries are based on dry soil, thus the present SOGM can only generate dry soil reflectance spectra as all training data only contain dry soil spectra. For modelling the soil reflectance as a function of the soil moisture content, a separate model was introduced.

The reflectance spectra of wet soil are typically a series corresponding to discrete soil moisture contents derived from the reflectance spectra of dry soil measurements [10, 11, 30]. Thus a regression model based on a 1D U-Net model [51] was used to determine the wet soil spectrum when the dry soil spectrum and soil moisture content values are provided. The output data of the model is the difference between dry and wet soil spectra. From this, the wet soil spectra can be obtained by subtracting this output from the dry spectra. Therefore, unlike the SOGM which can use flexible

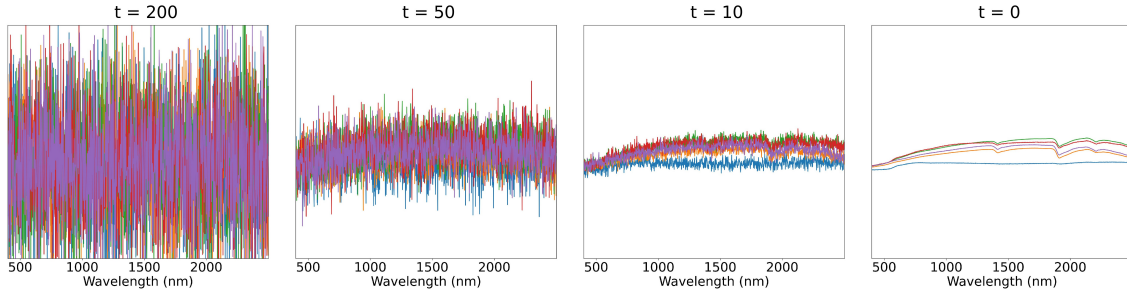


Figure 3: Example illustration of the spectral denoising process. During the reverse diffusion process, the soil spectra are progressively recovered as the time step decreases. Four example spectra are shown at time steps ( $t$ ): 200, 50, 10, and 0.

combinations of soil properties as input, the wet spectra model requires specific input data (i.e.,  $SMC_g$  and reference dry spectrum), making it a deterministic model without the variability inherent in the SOGM.

To align with the requirements of the model, the data from MARMIT2020 [10, 11] and Tian2021 [30] repositories were converted into 1670 samples, each of which contain a dry soil spectrum, a SMC value, and the corresponding wet soil spectrum. The dataset was randomly divided into 1300 training spectra, and 370 testing spectra.

## 2.6 Soil-plant image generation based on 3D ray-tracing model

Synthetic images of model scenes containing plants with soil background were generated using the Helios 3D plant modeling software (v1.3.0) [24]. The Helios software enables generation and manipulation of fully-resolved 3D geometric models of plants, the ground, or other objects. For example, plant canopy geometries of bean crops used in the present study were created using the Helios “Canopy Generator” plug-in. The procedural models have user-defined geometric parameters such as canopy height, leaf size, leaf area index (LAI), and leaf angle distribution, which allows for easy customization of the specifics of the canopy, and can be used as annotations for output images at both large and small scales. Users can also add external model geometries to the scene from standard polygon file formats. Geometry added to the scene can be referenced based on their unique identifiers in order to assign their spectral radiative properties.

In order to generate synthetic images, the distribution of absorbed, reflected, transmitted, and emitted radiation for all primitive elements in the scene is computed for a single scattering iteration based on the 3D ray-tracing method proposed by [53]. A ray-tracing-based camera model is then used to sample the reflected and transmitted energy for every camera pixel across all wave bands (Fig. 4). Scattering iterations continue for multiple scattering instances, and the camera continues accumulating scattered radiation until the amount of remaining scattered radiation becomes arbitrarily small. The camera also uses ray-tracing to determine primitive elements contained within each pixel, which is then used for image labeling. The radiation transport among objects and the

radiation received by the simulated camera sensor has been verified by using the RAMI On-line Model Checker [54] (ROMC, [https://romc.jrc.ec.europa.eu/\\_www/](https://romc.jrc.ec.europa.eu/_www/)).

Before running the ray tracing model, the optical properties, including the total hemispherical reflectivity  $\rho$  and transmissivity  $\tau$  across each radiative band, must be assigned to the corresponding geometric elements within the scene. These properties also incorporate the camera spectral response for the particular band. They can be calculated as:

$$\rho_o = \frac{\int_{\lambda_{min}}^{\lambda_{max}} \rho_{\lambda} C_{\lambda} S_{\lambda} d\lambda}{\int_{\lambda_{min}}^{\lambda_{max}} S_{\lambda} d\lambda}, \quad (2)$$

$$\tau_o = \frac{\int_{\lambda_{min}}^{\lambda_{max}} \tau_{\lambda} C_{\lambda} S_{\lambda} d\lambda}{\int_{\lambda_{min}}^{\lambda_{max}} S_{\lambda} d\lambda}, \quad (3)$$

where  $\lambda$  refers to the wavelength, and  $\lambda_{min}$  and  $\lambda_{max}$  represent the lower and upper bounds, respectively, of the selected waveband,  $C_{\lambda}$  is the spectral sensitivity of the camera sensor for wavelength  $\lambda$  (the whole camera spectral response is calibrated according to Appendix B), and  $\rho_{\lambda}$ ,  $\tau_{\lambda}$ , and  $S_{\lambda}$  are the spectral reflectivity, spectral transmissivity, and spectral source flux at wavelength  $\lambda$ , respectively. The  $\rho_{\lambda}$  of a soil primitive is one value in the soil reflectance spectrum  $\mathbf{R}_0$  at wavelength  $\lambda$  generated by the present SOGM (Fig. 4). The  $\rho_{\lambda}$  and  $\tau_{\lambda}$  of leaves can be generated by the PROSPECT-D [55] or PROSPECT-PRO model [56], which has been implemented into Helios. Alternatively,  $\rho_{\lambda}$ ,  $\tau_{\lambda}$ , and  $S_{\lambda}$  can be manually measured by using spectroscopic devices that cover the VIS-NIR range.

The model allows automatic annotation of generated images based on an arbitrary geometric grouping or any variable simulated in Helios. The annotation process starts by determining the unique identifiers of geometric element(s) contained in every pixel of the simulated image. Once these identifiers are known, any information about these primitives available in Helios (e.g., type, angle, area, computed fluxes) can be queried and used to generate “labelled” images.

## 2.7 Model performance evaluation

To verify the performance of the SOGM, the soil properties from testing datasets were input into the SOGM, and the generated spectra were compared against the corresponding real spectra from the testing datasets. As the generative model has uncertainty, the model was run 10 times with different random seeds, from which mean spectra were calculated to get relatively stable results for model evaluation. The generated mean spectra were then used for final evaluation. The testing spectra were padded using the present spectra padding model before comparison, and the performance of the spectra padding model was also evaluated. The wet soil spectra model was also evaluated by comparing the real and predicted wet soil spectra based on input SMCs and corresponding dry soil spectra. The root mean square error (RMSE) averaged across all spectra in the dataset was used to evaluate the absolute errors, as the values of reflectivity is an important physical parameter in

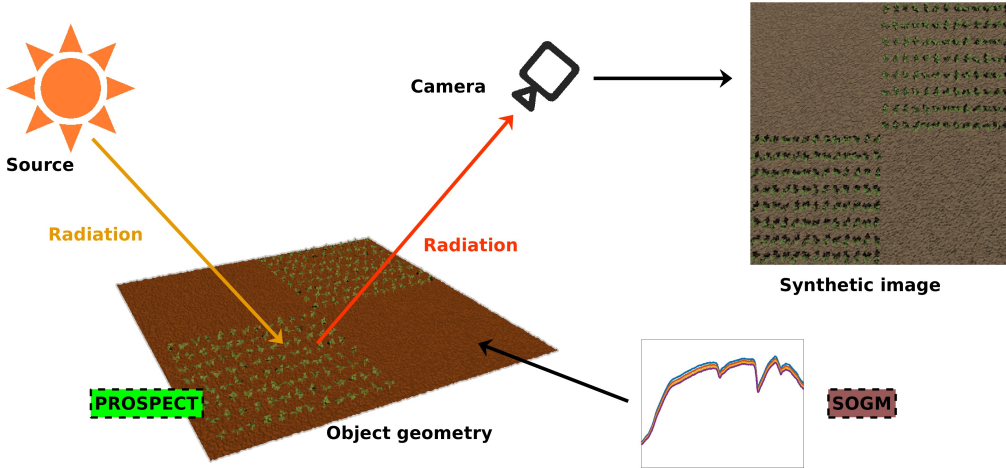


Figure 4: Schematic representation of the 3D radiation model for image generation. A ray-tracing-based camera model is used to simulate radiation that is emitted from a radiation source (e.g., sun, LED light) and reaches the camera after being scattered by objects in the scene. The PROSPECT-based leaf optical model and SOGM can generate the leaf and soil optical properties, respectively. Finally, the simulated camera generates resulting images that can be arbitrarily auto-annotated.

radiation transfer modelling. The mean square of Pearson’s correlation coefficient ( $r^2$ ) was used to evaluate the correlation between predicted and real spectra. The mean RMSE and  $r^2$  can be calculated as:

$$\text{RMSE} = \frac{1}{n} \sum_{i=1}^n \text{RMSE}_i, \quad (4)$$

$$r^2 = \frac{1}{n} \sum_{i=1}^n r_i^2, \quad (5)$$

where  $\text{RMSE}_i$  and  $r_i^2$  are the root mean square error and square of correlation coefficient of the  $i$ -th pair of generated and real spectra, respectively.

The soil colors in generated soil images were also evaluated based on a photo from [1]. The mean color RGB values of all pixels for one type of soil from real and synthetic soil images were used for comparison. As the light and camera details are not provided in the original literature (which are required inputs for the camera model), only  $r^2$  was used for evaluation as it gives a relative rather than absolute measure of agreement.

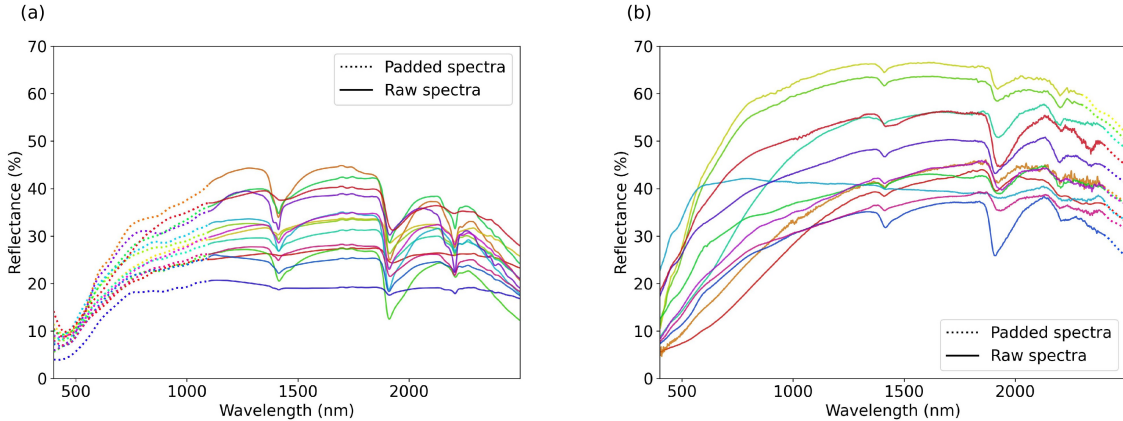


Figure 5: Full-range spectra obtained by applying the spectra padding model to (a) Barthès2023 and (b) MARMIT2020 datasets. The solid curves represent the original spectra, and the dotted curves are the reconstructed portion of the spectra.

### 3 Results

#### 3.1 Spectra padding

The wavelength range of the Barthès2023 and Hu2020 datasets spans from 1100 to 2499 nm and 400 to 2499 nm, respectively. The wavelength range of MARMIT2020 [10, 11] extends from 400 nm to approximately 2349 - 2449 nm, as it contains spectral data from multiple sources. The missing wavelengths between 400 and 2499 nm were reconstructed using the present spectra padding model.

Figure 5 shows some padded spectra from Barthès2023 and MARMIT2020 data sets, and the padding overall looks reasonable based on visual inspection. Nevertheless, the accuracy of these padding results cannot be evaluated, as the missing parts were not provided by the original datasets. Thus, to verify the performance of the spectra padding model, spectral bands 400-799 nm, 400-1099 nm, and 2100-2499 nm were set to 0, and the model was used to predict these zero-set bands based on the remaining values. Table 4 displays the error metrics for all three selected wavebands, which indicated good performance for both the Hu2020 and MARMIT2020 datasets (RMSE < 3 and  $r^2 > 0.8$ ). It should be noted that not all spectral bands within 2100-2499 nm in MARMIT2020 dataset are evaluated, as some spectra do not fully cover this range. These results of 400-1099 nm and 2100-2499 nm indicate the reconstructed missing parts of Barthès2023 and MARMIT2020 (Fig. 5) are reliable. The spectral bands 400-799 nm and 400-1099 nm are missing in the original Barthès2023 dataset, thus these results are unavailable in Table 4. The RMSE for the 2100-2499 nm range in the Barthès2023 dataset is higher than that of the other two datasets. This is reasonable, as it only utilizes the spectral band from 1100-2099 nm (1000 wavelengths) to reconstruct the missing part, which is fewer than the wavelengths (1700) used in the other two datasets.

Table 4: Evaluation of spectra padding model based on spectral datasets listed in Table 2. Reflectance values were set to 0 across 3 target wavebands, and the padding model was used to reconstruct the zeroed values.

Target waveband	Barthès2023		Hu2020		MARMIT2020	
	RMSE	$r^2$	RMSE	$r^2$	RMSE	$r^2$
400-799 nm	-	-	1.68	1.00	2.81	0.96
400-1099 nm	-	-	1.95	1.00	3.07	0.96
2100-2499 nm	3.54	0.66	2.18	0.92	2.06	0.81

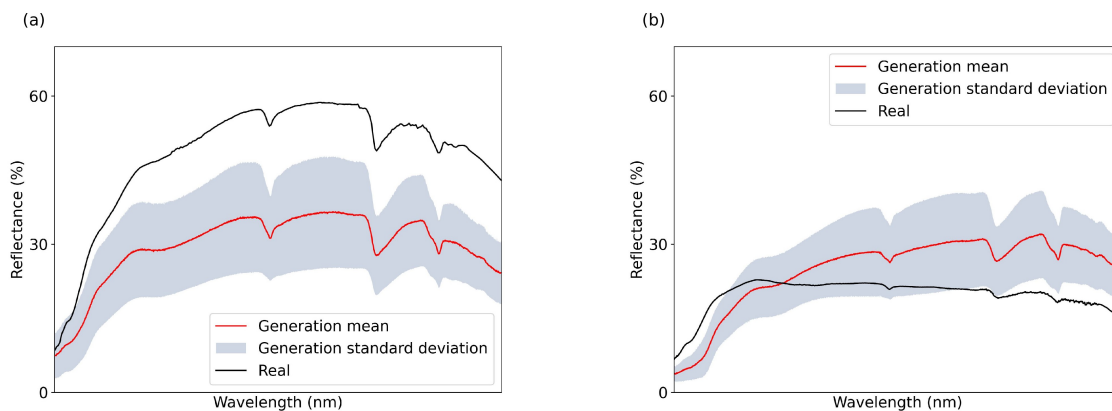


Figure 6: Example real soil reflectance spectra and mean and standard deviation of generated soil reflectance spectra with similar soil particle fraction properties and spectrometer manufacturer (ASD). (a) Clay : 22.0%; Silt : 26.0%; Sand : 52.0%. (b) Clay : 17.3%; Silt : 26.1%; Sand : 56.6%.

### 3.2 Spectra generation

When all available input properties are provided to the model, the RMSE for the Barthès2023 dataset was 5.52% (Table 5) with an  $r^2$  of 0.86. Excluding the input information of spectrometer manufacturer leads to larger errors for all three datasets, which means the model effectively learned the spectral variation caused by different spectrometer manufacturers from the training datasets without ever seeing these test datasets. For datasets Barthès2023 and MARMIT2020, randomly dropping one or two input properties led to increased errors, which is intuitively expected. Figure 6 shows spectra from two example soil samples with similar clay, silt, and sand fractions, yet they exhibit very different optical properties. Consequently, if only these properties are input into the SOGM, the model can predict a spectrum that is “reasonable”, but more information is needed to accurately describe the soil spectra. In the case of Barthès2023, the RMSE is 5.92% when only particle size information (clay, silt, and sand fraction) is input. Adding nitrogen and organic carbon improves the RMSE to 5.19% and 5.69%, respectively, as shown in Table 5.

Interestingly, for the dataset Hu2020, randomly reducing the number of input properties actually

Table 5: Error in soil spectra generative model predictions based on variable combinations of input properties. The model was trained based on the spectral datasets listed in Table 1, and then used to predict the spectral datasets Barthès2023, Hu2020 and MARMIT2020 (Table 2) based on variable input parameters. Error between predicted and true spectral reflectance was quantified by RMSE (%) and  $r^2$ .  $n$  denotes the number of spectra considered.

Dataset	Barthès2023			Hu2020			MARMIT2020		
Property	RMSE	$r^2$	$n$	RMSE	$r^2$	$n$	RMSE	$r^2$	$n$
All	5.52	0.86	404	12.91	0.90	47	13.54	0.92	201
- Manufacturer	6.20	0.81	404	13.34	0.92	47	14.17	0.90	201
- 1	6.48	0.79	404	11.43	0.94	47	13.98	0.92	201
- 2	6.60	0.79	404	11.71	0.94	47	14.69	0.90	201
Particle	5.92	0.90	229	9.98	0.97	46	14.92	0.90	185
OC	6.26	0.85	404	-	-	-	11.56	0.92	99
Particle & OC	5.69	0.90	229	-	-	-	11.69	0.94	92
Fe	-	-	-	12.08	0.94	47	12.01	0.88	104
Particle & Fe	-	-	-	9.76	0.97	46	10.63	0.92	101
Particle & Fe & Mg	-	-	-	9.69	0.97	46	-	-	-
Particle & Fe & Ni	-	-	-	12.39	0.94	40	-	-	-
Density	6.96	0.77	404	-	-	-	10.35	0.92	16
Particle & Density	5.96	0.85	229	-	-	-	14.94	0.97	2
N	6.11	0.81	404	-	-	-	12.27	0.94	3
Particle & N	5.19	0.90	229	-	-	-	12.66	0.90	2
SOM	-	-	-	-	-	-	13.80	0.90	107
Particle & SOM	-	-	-	-	-	-	12.45	0.92	104
OC & SOM & CaCO <sub>3</sub>	-	-	-	-	-	-	11.13	0.92	95
Particle & OC & SOM & CaCO <sub>3</sub>	-	-	-	-	-	-	11.14	0.94	92

Soil property input abbreviations: All: all available soil properties; -Manufacturer: all available properties except spectrometer manufacturer; -1 and -2: all available properties except one or two soil properties are randomly omitted (if omission leaves only one remaining property, no properties will be dropped); Particle: clay, sand, and silt contents; OC: organic carbon content; Fe: total iron content; Mg: total magnesium content; Ni: total nickel content; Density: bulk density; N: total nitrogen content; SOM: soil organic matter content.

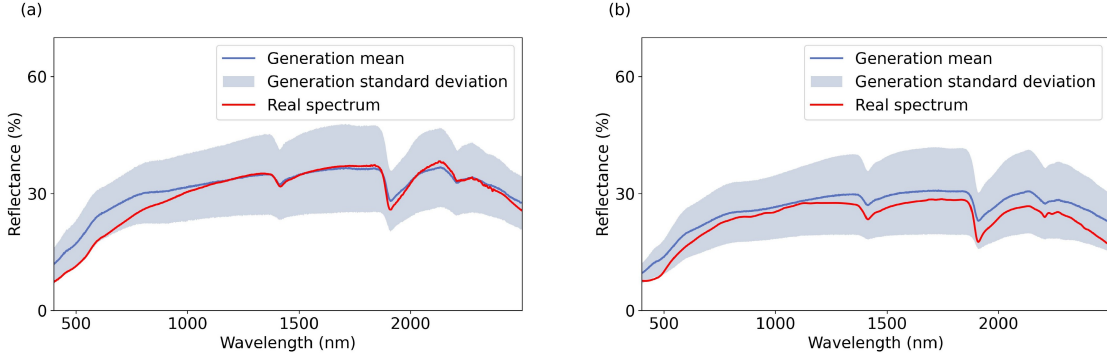


Figure 7: Variability in predicted soil reflectance spectra based on incomplete inputs. Real soil spectra are compared against the distribution of 10 generated spectra based on soil properties of (a) Spectrometer manufacturer: ASD, Clay: 45.7 %, Silt: 34.8 %, Sand: 19.4 %, Soil organic matter: 14.6 g/kg, CaCO<sub>3</sub> content: 36 g/kg, Total iron content: 40700.0 mg/kg, Organic carbon content: 8.5 g/kg; (b) Spectrometer manufacturer: Spectral Evolution, Clay: 62.9 %, Sand: 20.0 %, Silt: 17.1 %, Bulk density: 1.036 g/cm<sup>3</sup>, Organic carbon content: 18.9 g/kg, Total nitrogen content: 1.57 g/kg.

led to better results. This result is reasonable when the input properties of this dataset are considered, since this dataset contains many elements with low concentration ( $<0.1\%$ ) such as nickel and zinc. These minority elements have relatively higher measurement error, and also appeared a few times in the training datasets. For these reasons, including such properties as inputs may have a negative effect on model performance. If only the particle fraction property is input into the model, the resulting RMSE of 9.98% and  $r^2$  of 0.97 is much better than when all input properties are included (Table 5). Adding iron and magnesium inputs can further improve model performance, as these two elements have relatively high concentration around 1~5%. However, adding nickel (content  $<0.005\%$ ) tends to increase overall model error.

There is uncertainty and random variability in the SOGM spectra generation, which is a trade-off to the model's ability to predict reasonable spectra with incomplete inputs. Figure 7 presents real soil spectra alongside the distribution of 10 generated spectra based on the same property inputs. The generated mean spectra fall within a more acceptable range than generated mean spectra shown in Fig. 6, as more soil properties are provided. In general, averaging is recommended to reconstruct a stable spectrum. For other purposes, such as image generation or soil property estimation, averaging may not be necessary, as the generation uncertainty can contribute to greater data variation. Furthermore, by using the same random seeds, the model can also generate a series of soil spectra based on a gradient in soil properties.



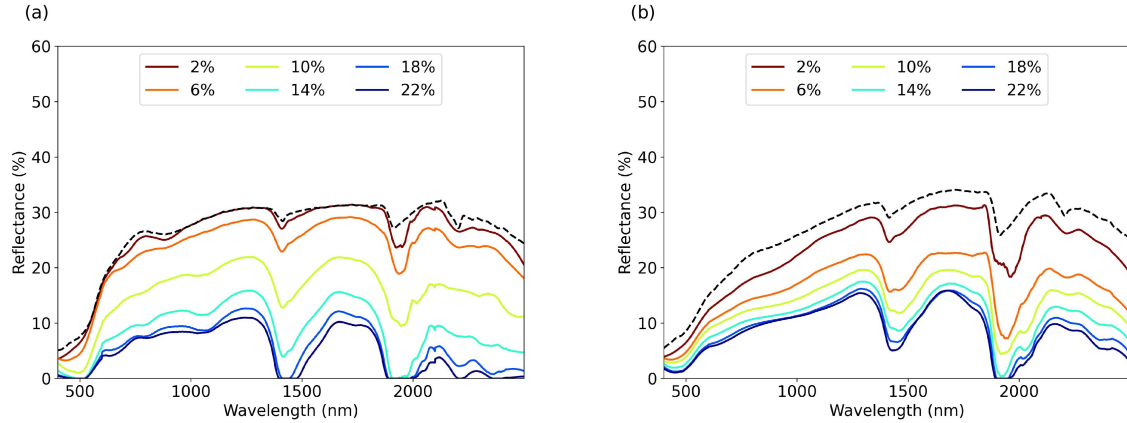


Figure 8: Wet soil reflectance spectra predicted by the wet soil spectra model based on dry soil spectra (black dotted lines) randomly generated by the SOGM. The values in the figure legends are the input soil moisture content (%).

### 3.3 Wet soil spectra

The soil moisture model achieved an RMSE of 3.19% and  $r^2$  of 0.90 on the 370 wet soil spectra testing set. While these errors are relatively low, the result can potentially be improved further by increasing the model parameters and number of training iterations. However, the number of spectra available for training the wet spectra model was much smaller than that used for the (dry) SOGM. Therefore, training was stopped at 5000 iterations to prevent overfitting. It was observed that additional training iterations could achieve lower errors on the testing set, but when the model trained with  $>5000$  iterations was applied to unseen generated spectra, spectra with smaller moisture content could have lower overall reflectance than those with larger moisture content, which is not in line with reality.

The SOGM was then coupled with the wet soil model by using the dry spectra generated by the SOGM as input to the wet soil model (Fig. 8). Figure 8 shows wet soil reflectance spectra predicted by the wet spectra model based on several input SMCs and two dry soil spectra randomly generated by the SOGM. Eventually, the integration of SOGM with the wet spectral model enables SOGM to generate wet soil spectra.

### 3.4 Synthetic soil images

Figure 9 shows synthetic soil-plant images generated using the Helios 3D plant modelling software [24]. The soil reflectance spectra used for soil radiative property inputs were generated by the SOGM (average of 5 spectra) based on different input soil properties, which are shown in Fig. 13a. For Fig. 9a, the soil model input properties were determined based on *Terra Preta* soil as described in [57] and [58]. *Terra Preta* soil is nearly black in color, which is reproduced in the synthetic image

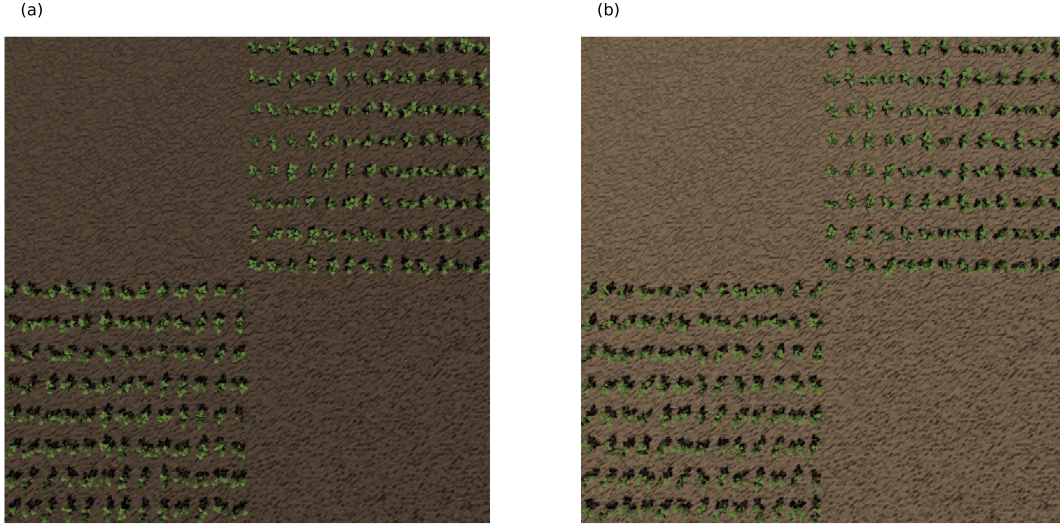


Figure 9: Synthetic soil-plant images based on soil properties of (a) *Terra Preta* soil: Clay: 8 %, Silt: 7 %, Sand: 85 %, Soil organic matter: 120 g/kg, Total iron content: 80000 mg/kg, Organic carbon content: 38 g/kg, Cation exchange capacity: 123 cmol(+)/kg, pH measured from water: 4.7; (b) soil near Davis, CA, USA: Clay: 33 %, Silt: 47 %, Sand: 20 %, Soil organic matter content: 30 g/kg, Organic carbon content: 8 g/kg, Electrical conductivity 55 mS/m, pH measured from water: 6.8, Cation exchange capacity: 30 cmol(+)/kg). These scenes were illuminated by simulated sun light using the ASTM standard clear sky solar spectrum distribution with solar zenith angle of  $20^\circ$ . A simulated Nikon B500 camera (Nikon, Minato City, Tokyo, Japan) was used for imaging, and the camera response spectra used is shown in Fig. 13b.

(Fig. 9a). The soil model input properties for Fig. 9b were determined based on soil properties near Davis, CA, United States recorded in the Soil Survey Geographic (SSURGO) Database. More specific details regarding input soil parameters are given in the figure captions corresponding to each image.

Figure 10 displays a synthetic image featuring one type of soil with different SMCs, along with its corresponding SMCs distribution map. Since users can specify the soil properties, the 3D ray-tracing model labels the soil image at the pixel scale, which can be used as training data for machine learning models.

Figure 11a shows synthetic soil images based on properties reported by [1] and corresponding real soil images. As is normally the case, the lighting type and camera model used to create the real soil photographs was not reported. We therefore assumed that the soil samples were illuminated by 4 Cree XLamp XHP70.2 LED light sources, and that a Basler ace acA2500-20gc RGB camera (Basler, Ahrensburg, Germany) was used to capture the image. The generated soil reflectance spectra and simulated camera spectra responses are shown in Fig. 14. The synthetic red color values of soil sample AZ4B and AZ11 are lower than their actual red color values, which is a primary factor in the visual differences observed between their real and synthetic soil images. This discrepancy may

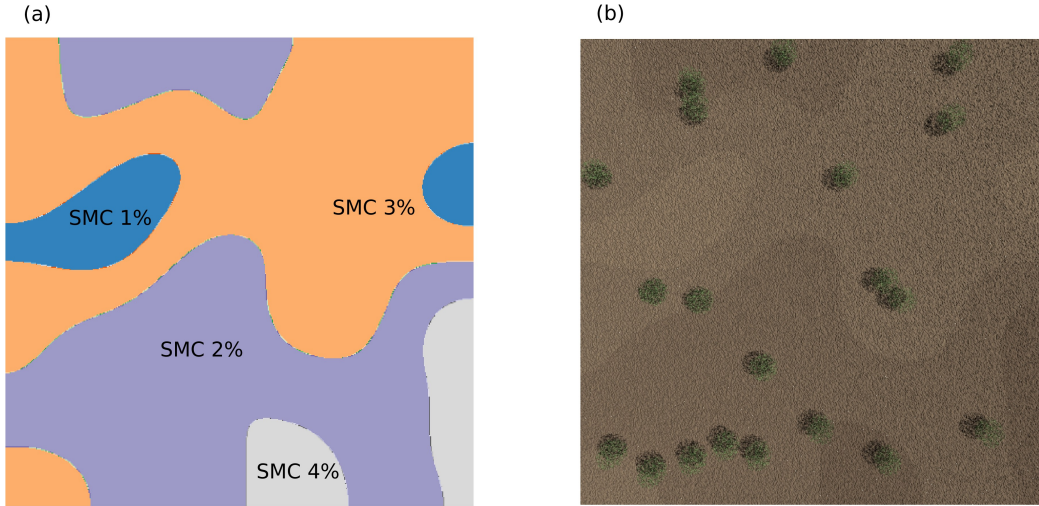


Figure 10: (a) Soil SMC distribution map. (b) Synthetic soil image based on soil spectra affected by corresponding SMCs.

be due to the absence of specific light and camera settings, particularly the bias of the red camera spectral response and blue peak in the LED light source spectrum. Additionally, there is a noticeable difference between the real and synthetic green and blue color values for soil sample AZ18 (Fig. 11), which is likely caused by the limited soil properties provided by [1]. Despite these limitations, the synthetic color values derived from the simulated soil images still exhibit a high  $r^2$  of 0.86 with actual color values. This demonstrates the robustness and accuracy of the spectra generated by SOGM and images simulated by the Helios ray-tracing model.

## 4 Discussion

The present SOGM can generate soil spectra based on a wide range of soil properties such as particle size, organic matter content, organic carbon content, total nitrogen content, iron content, cation-exchange capacity, pH value, bulk density, and SMCs. The biggest contribution of the present work is to build a model that can encode most of the soil reflectance spectra-property data available online through a text-based generative model, and remove the barrier due to data non-uniformity such between mass-based and volumetric concentrations. Many radiative transfer based models that can simulate soil reflectance spectra in the VIS-NIR region rely on only one or a few properties, which mainly focus on soil moisture [10, 11, 59, 13], particle size [1, 12], and organic matter [12]. Compared to these models, the SOGM offers greater flexibility by accepting any combination of soil properties as inputs. When the input soil property set is incomplete, the model generates a spectrum that is reasonable within the constraints of available parameters. As a more complete property set is input to the model, uncertainty in the model is reduced and the generated spectrum becomes more

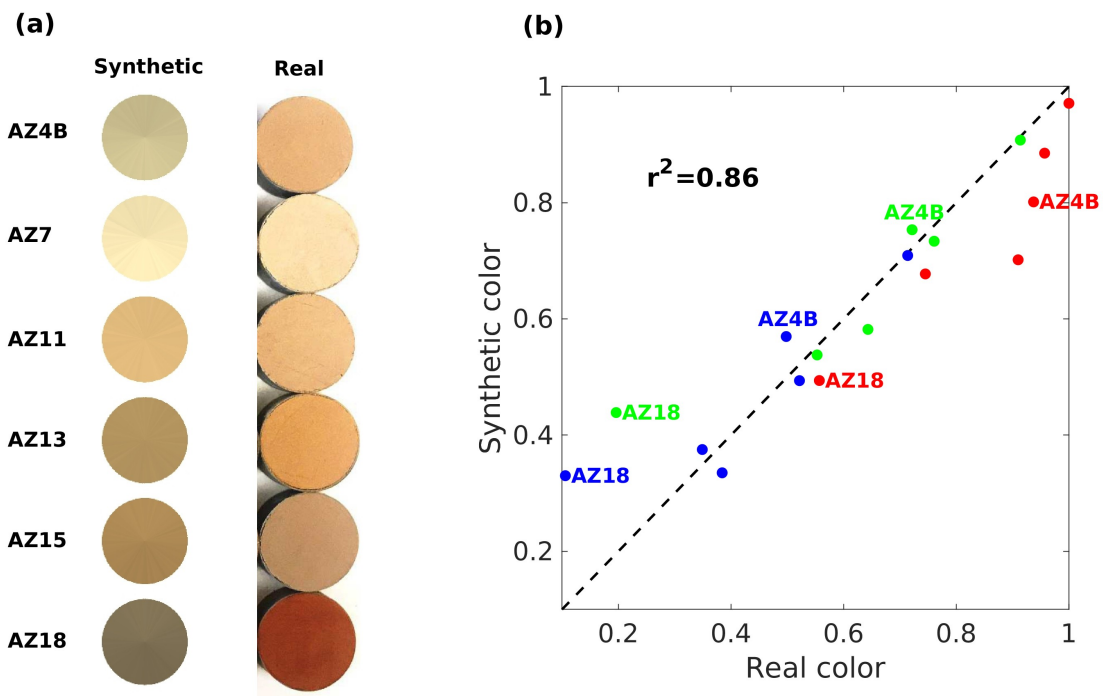


Figure 11: Comparison of real and synthetically generated images of soil samples with different properties. (a) Real soil images from [1] (right) compared against synthetic images generated using Helios with soil reflectance spectra generated from the SOGM (left). The synthetic image was generated based on properties provided in the original paper [1] can be found in Table 6. Sample IDs are also in accordance with those provided in the paper. (b) Real and synthetic soil RGB values represent the mean pixel values of corresponding soil sample regions, scaled from 0~255 to 0~1. Data points for samples AZ4B and AZ18 are labeled for comparison against the images in (a).

constrained.

The SOGM was tested on three datasets that were not included in the training process, which produced good results. Although the performance of wet soil spectra simulations was not as good as the multilayer radiative transfer model of soil reflectance (MARMIT) [10] and MARMIT2 [11], the present model can be directly applied on new dry soil spectra without extracting specific model parameters. By combining with the 3D ray-tracing model in Helios, soil images can also be generated based on available soil properties to generate soil that appears reasonable based on these properties.

Apart from soil research, the current model can enable investigation of a variety of radiation-dependent soil-plant interactions by combining the SOGM with other radiation modeling tools such as Helios [24] and PROSAIL [4]. The Helios 3D modeling software has sub-models for plant biophysical processes, thus adding the SOGM can allow for generalized specification of soil optical properties in order to improve representation of plant-soil interactions. Furthermore, the 3D ray-tracing model in Helios supports automatic image annotation (allowing the assignment of traits to individual pixels) that incorporates multiple plant traits such as plant height, leaf chemical concentrations, plant or leaf ID for object detection, etc. Adding the SOGM can further extend the capabilities to soil property labelling. Although not explicitly investigated in present study, the synthetic images can serve as inputs to machine learning models designed for remote and proximal sensing studies. While the example applications focused on RGB imagery datasets, another important strength of the proposed modeling framework is that it can simulate other sensor modalities such as multispectral imagery. The reflectance spectra can be integrated across arbitrary wavelength bands or camera spectral response curves. The integration of the current SOGM with the PROSAIL model [4] is straightforward, with details provided in Appendix A. As the soil reflectance generation is based on a wide range of user-specified properties, this combination may enable many potential remote sensing studies linking soil properties to complex surface radiative properties.

The SOGM has some limitations that should be considered during its application. Since the model is data-driven, inaccuracies in the training data can translate into inaccuracy in model predictions. Most notably, certain minor soil properties with low concentration such as nickel might adversely affect spectra generation due to their high propensity for measurement errors and small influence on soil spectra (Table 5). This can be mitigated by removing these properties from the list of inputs when possible. Additionally, there is a lack of wet soil spectra available in public spectral repositories, leading to relatively high prediction errors for the wet soil spectra model. Increasing the availability of open spectral datasets could help mitigate these limitations in the future.

## 5 Conclusion

In this research, we introduced the SOGM, an new model for generating soil VIS-NIR reflectance spectra based on incomplete input physical properties with variable formats. The model’s capability to encode a vast array of soil spectra-property data available online through a text-based generative approach sets it apart from existing models, overcomes the limitations of data incompatibility barriers, and offers the flexibility to process various combinations of soil attributes, including soil moisture, without any additional model parameters.

This work demonstrated the possibility of using a data-driven approach for modeling soil reflectance based on diverse and incomplete datasets. Through testing of the SOGM on new datasets not included in model training, this work demonstrated that the model can generate reasonable soil reflectance spectra based on available property inputs, which can be improved and constrained as the input parameter set increases (although this may not always be the case depending on the accuracy of the input property measurements). Results suggested that the most widely used soil properties, including particle composition (clay/sand/silt), bulk density, organic carbon, organic matter, and total nitrogen contents tended to improve soil reflectance predictions when available. Properties such as nickel content tended to decrease model performance due to their relatively low concentrations and elevated propensity for measurement error.

The integration of the SOGM with a radiation-based image simulator such as Helios, Large-Scale remote sensing data and image simulation framework (LESS) [60], and the Discrete Anisotropic Radiative Transfer (DART) Lux model [61, 62] enables the generation of realistic soil images based on diverse soil properties. This combination paves the way for comprehensive studies in soil-plant interactions. The potential of our model in supporting remote sensing studies, particularly when integrated with the soil-plant radiative models such as PROSAIL model, is noteworthy. Despite some limitations, such as the impact of certain soil properties on spectra generation and the scarcity of wet soil spectra data, the SOGM represents a substantial step forward in soil spectra simulation.

This study not only contributes to the advancement of soil spectra generation but also opens new ways for future exploration and innovation in the field of ecosystem and agriculture.

## Declaration of Competing Interest

The authors declare that they have no known competing financial interests or personal relationships that could have appeared to influence the work reported in this paper.

## Acknowledgements

This work was supported, in whole or in part, by the Bill & Melinda Gates Foundation INV-0028630. Under the grant conditions of the Foundation, a Creative Commons Attribution 4.0 Generic License has already been assigned to the Author Accepted Manuscript version that might arise from this submission.

## Appendix A Integration with the PROSAIL model

The PROSAIL model is a fusion of the PROSPECT-based models [63, 55, 64] and SAIL-based models [65, 66]. The 4SAIL model can be depicted mathematically as:

$$\mathbf{R}_{\text{surface}} = 4\text{SAIL}(\mathbf{R}_{\text{leaf}}, \mathbf{T}_{\text{leaf}}, \text{LAI}, \text{LIDF}, S_L, \theta_s, \theta_v, \mathbf{R}_{\text{soil}}), \quad (6)$$

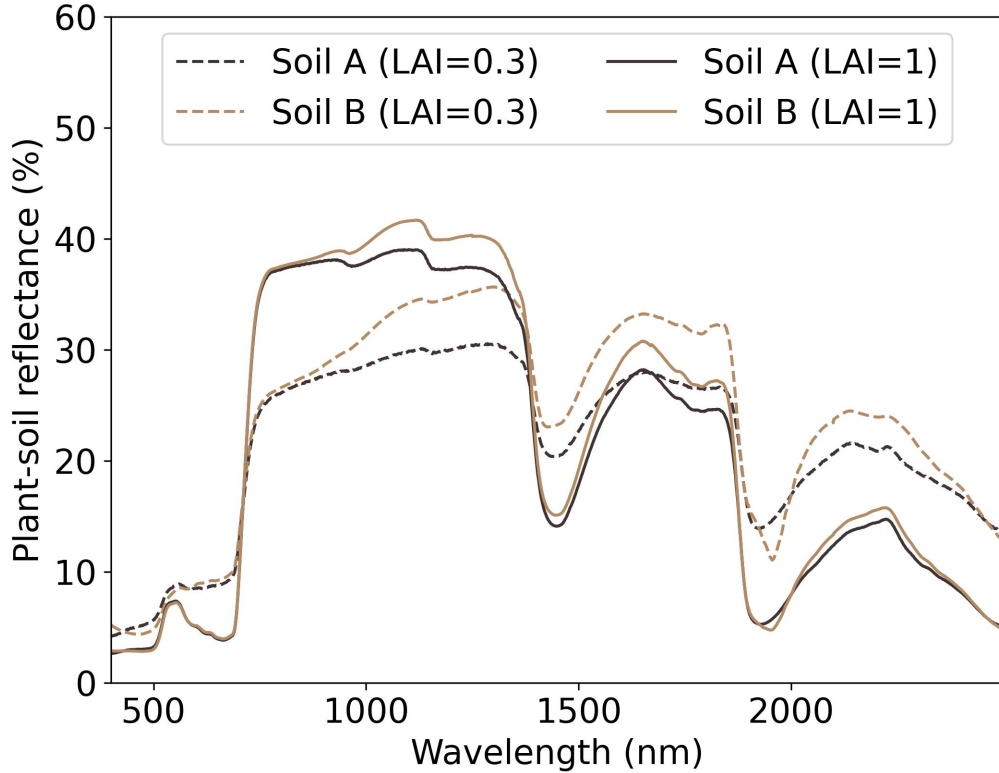


Figure 12: Soil A and B use the input properties corresponding to those in Fig. 13a and Fig. 13b, respectively. Other PROSAIL inputs include: the number of elementary layers set to 1.5, chlorophyll concentration at  $40 \mu\text{g}/\text{cm}$ , carotenoid concentration at  $8 \mu\text{g}/\text{cm}$ , equivalent water thickness at  $0.01 \text{ g}/\text{cm}$ , dry matter content at  $0.009 \text{ g}/\text{cm}$ , and Solar zenith angle at  $30^\circ$ . Two LAI value, 0.3 and 1, are employed for the simulations of two different soil-plant surface spectra.

where  $\mathbf{R}_{\text{surface}}$  is the surface reflectance spectra,  $\mathbf{R}_{\text{leaf}}$  and  $\mathbf{T}_{\text{leaf}}$  are leaf reflectance and transmittance spectra, which are obtained using the PROSPECT-based models by specifying leaf chemical properties such as chlorophyll concentration, carotenoid concentration, water concentration etc., LIDF represents the leaf inclination distribution function containing one or two parameters,  $S_L$  is the hot spot parameter,  $\theta_s$  and  $\theta_v$  denote solar and viewing zenith angle, respectively, and  $\mathbf{R}_{\text{soil}}$  is the soil Lambertian reflectance spectra, which can be easily generated by our SOGM. Figure 12 shows example soil-plant spectra simulation using the integration of SOGM and PROSAIL model.

## Appendix B Camera spectral responses

Figure 13a and 14a display soil reflectance spectra generated by SOGM, which were used to simulate soil-plant images in Fig. 9 and 11, respectively. Given that the target images are in RGB bands, only the spectra within the visible region 400-800 nm are presented.

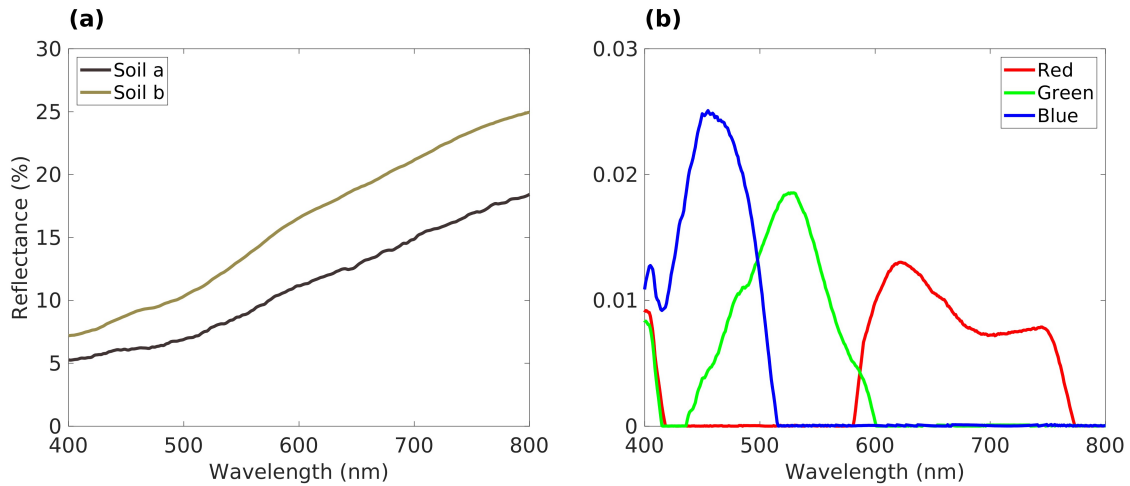


Figure 13: (a) Synthetic soil spectra in visible region (400-800 nm) for generating synthetic soil image Fig. 9. (b) Calibrated Nikon B500 camera spectral responses.

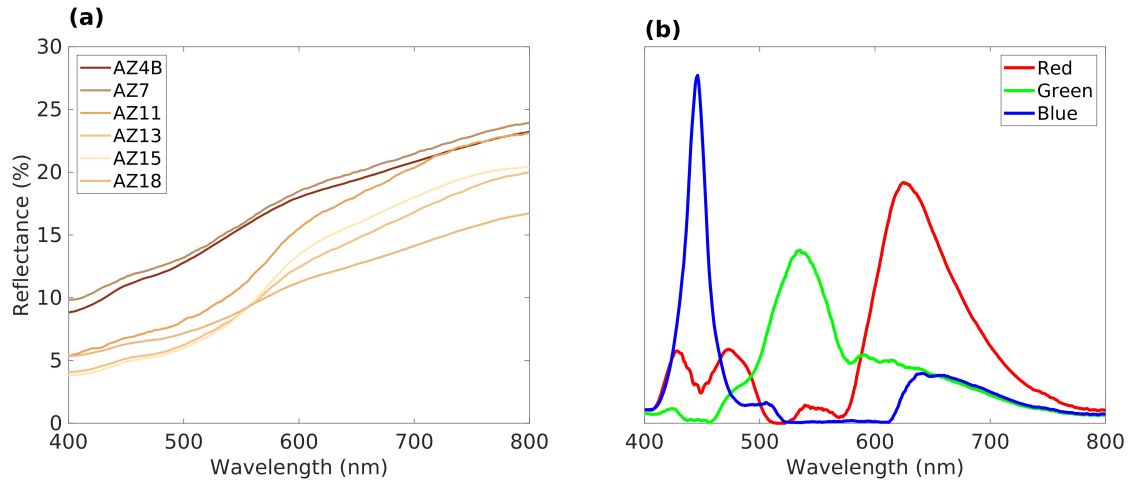


Figure 14: (a) Synthetic soil spectra based on properties provided by [1]'s literature in visible region (400-800 nm) for generating synthetic soil image Fig. 11a. (b) Calibrated Basler ace acA2500-20gc RGB camera spectral responses.



Figure 13b and 14b present the calibrated Nikon B500 (Nikon, Minato City, Tokyo, Japan) and Basler ace acA2500-20gc RGB (Basler, Ahrensburg, Germany) camera spectral responses used for generating Fig.9 and Fig. 11a, respectively. Table 6 showcases the soil properties provided by [1]’s paper used for simulating corresponding soil spectra.

Table 6: Soil Properties provided in [1]’s paper.

Soil Code	Bulk densities (g/cm <sup>3</sup> )	Sand (%)	Silt (%)	Clay (%)	Organic Matter (%)
AZ4B	1.528	80.4	14.2	5.4	2.3
AZ7	1.313	58.5	32.0	9.5	1.1
AZ11	1.398	38.5	40.1	21.4	1.7
AZ13	1.256	58.1	15.4	26.5	2.8
AZ15	1.025	3.6	73.4	23.0	3.4
AZ18	1.161	29.1	18.7	52.2	4.0

The Nikon B500 camera spectral response was calibrated based on a DKC-Pro color board image (DGK Color Tools, Boston, Massachusetts, USA) under real sun. The Basler ace acA2500-20gc RGB camera spectral response was calibrated based on a SpyderCHECKR 24 color board image (Datacolor, Risch-Rotkreuz, Switzerland) illuminated by 4 Cree XLamp XHP70.2 LED light sources.

## References

- [1] Morteza Sadeghi, Ebrahim Babaeian, Markus Tuller, and Scott B Jones. Particle size effects on soil reflectance explained by an analytical radiative transfer model. *Remote Sensing of Environment*, 210:375–386, 2018.
- [2] Jing Yuan, Xin Wang, Changxiang Yan, Shengbo Chen, Shurong Wang, Junqiang Zhang, Zhengyuan Xu, Xueping Ju, Ning Ding, Youzhi Dong, et al. Wavelength selection for estimating soil organic matter contents through the radiative transfer model. *IEEE Access*, 8:176286–176293, 2020.
- [3] Wout Verhoef and Heike Bach. Coupled soil–leaf–canopy and atmosphere radiative transfer modeling to simulate hyperspectral multi-angular surface reflectance and toa radiance data. *Remote Sensing of Environment*, 109(2):166–182, 2007.
- [4] Stéphane Jacquemoud. Inversion of the PROSPECT+ SAIL canopy reflectance model from AVIRIS equivalent spectra: theoretical study. *Remote Sensing of Environment*, 44(2-3):281–292, 1993.
- [5] Christiaan van der Tol, Micol Rossini, Sergio Cogliati, Wouter Verhoef, Roberto Colombo, Uwe Rascher, and Gina Mohammed. A model and measurement comparison of diurnal cycles of sun-induced chlorophyll fluorescence of crops. *Remote Sensing of Environment*, 186:663–677, 2016.

- [6] Peiqi Yang, Christiaan van der Tol, Tiangang Yin, and Wout Verhoef. The spart model: A soil-plant-atmosphere radiative transfer model for satellite measurements in the solar spectrum. *Remote Sensing of Environment*, 247:111870, 2020.
- [7] Qiaomin Chen, Bangyou Zheng, Karine Chenu, Pengcheng Hu, and Scott C Chapman. Un-supervised plot-scale lai phenotyping via uav-based imaging, modelling, and machine learning. *Plant Phenomics*, 2022.
- [8] Qiaomin Chen, Bangyou Zheng, Tong Chen, and Scott C Chapman. Integrating a crop growth model and radiative transfer model to improve estimation of crop traits based on deep learning. *Journal of Experimental Botany*, 73(19):6558–6574, 2022.
- [9] Deepak Upreti, Wenjiang Huang, Weiping Kong, Simone Pascucci, Stefano Pignatti, Xianfeng Zhou, Huichun Ye, and Raffaele Casa. A comparison of hybrid machine learning algorithms for the retrieval of wheat biophysical variables from sentinel-2. *Remote Sensing*, 11(5):481, 2019.
- [10] Aurelien Babelt, PVH Vu, Stéphane Jacquemoud, Françoise Viallefont-Robinet, Sophie Fabre, Xavier Briottet, Morteza Sadeghi, Michael L Whiting, Frédéric Baret, and Jia Tian. Marmit: A multilayer radiative transfer model of soil reflectance to estimate surface soil moisture content in the solar domain (400–2500 nm). *Remote Sensing of Environment*, 217:1–17, 2018.
- [11] Alice Dupiau, S Jacquemoud, Xavier Briottet, Sophie Fabre, Françoise Viallefont-Robinet, W Philpot, C Di Biagio, M Hébert, and P Formenti. Marmit-2: An improved version of the marmit model to predict soil reflectance as a function of surface water content in the solar domain. *Remote Sensing of Environment*, 272:112951, 2022.
- [12] Fuyu Wu, Kun Tan, Xue Wang, Jianwei Ding, Zhaoxian Liu, and Bo Han. A semi-analytical radiative transfer model for explaining soil spectral features. *International Journal of Applied Earth Observation and Geoinformation*, 118:103250, 2023.
- [13] H Bach and W Mauser. Modelling and model verification of the spectral reflectance of soils under varying moisture conditions. In *Proceedings of IGARSS'94-1994 IEEE International Geoscience and Remote Sensing Symposium*, volume 4, pages 2354–2356. IEEE, 1994.
- [14] Jing Yuan, Chunhui Hu, Changxiang Yan, Zhizhong Li, Shengbo Chen, Shurong Wang, Xin Wang, Zhengyuan Xu, and Xueping Ju. Semi-empirical soil organic matter retrieval model with spectral reflectance. *IEEE Access*, 7:134164–134172, 2019.
- [15] Fuyu Wu, Kun Tan, Xue Wang, Jianwei Ding, and Zhaoxian Liu. A novel semi-empirical soil multi-factor radiative transfer model for soil organic matter estimation based on hyperspectral imagery. *Geoderma*, 437:116605, 2023.
- [16] Gergely Toth, Arwyn Jones, Luca Montanarella, Christine Alewell, Cristiano Ballabio, Florence Carre, Delphine de Brogoniez, Rannveig Anna Guicharnaud, Ciro Gardi, Tamas Hermann, et al. *LUCAS Topsoil Survey-methodology, data and results*. 2013.

- [17] José A. M. Demattê, Jean Jesus Novais, Nicolas Augusto Rosin, Jorge T. F. Rosas, Raul Roberto Poppiel, André Carnieletto Dotto, and Ariane F. S. Paiva. The Brazilian Soil Spectral Library (VIS-NIR-SWIR- MIR) Database: Open Access, July 2023.
- [18] Arwyn Jones, O Fernandez-Ugalde, and Simone Scarpa. Lucas 2015 topsoil survey. *Presentation of Dataset and Results, EUR*, 30332, 2020.
- [19] J. L. Safanelli, T. Hengl, J. Sanderman, and L. Parente. Open soil spectral library (training data and calibration models), 2021.
- [20] Tong Lei and Da-Wen Sun. Achieving joint calibration of soil vis-nir spectra across instruments, soil types and properties by an attention-based spectra encoding-spectra/property decoding architecture. *Geoderma*, 405:115449, 2022.
- [21] Barry D Ganapol, Lee F Johnson, Christine A Hlavka, David L Peterson, and Barbara Bond. Lcm2: A coupled leaf/canopy radiative transfer model. *Remote Sensing of Environment*, 70(2):153–166, 1999.
- [22] Jonathan Ho, Ajay Jain, and Pieter Abbeel. Denoising diffusion probabilistic models. *Advances in Neural Information Processing Systems*, 33:6840–6851, 2020.
- [23] Robin Rombach, Andreas Blattmann, Dominik Lorenz, Patrick Esser, and Björn Ommer. High-resolution image synthesis with latent diffusion models. In *Proceedings of the IEEE/CVF Conference on Computer Vision and Pattern Recognition*, pages 10684–10695, 2022.
- [24] Brian N Bailey. Helios: A scalable 3D plant and environmental biophysical modeling framework. *Frontiers in Plant Science*, 10:1185, 2019.
- [25] Rosa Oltra-Carrió, Frédéric Baup, Sophie Fabre, Rémy Fieuzal, and Xavier Briottet. Improvement of soil moisture retrieval from hyperspectral vnir-swir data using clay content information: From laboratory to field experiments. *Remote Sensing*, 7(3):3184–3205, 2015.
- [26] Audrey Lesaignoux, Sophie Fabre, and Xavier Briottet. Influence of soil moisture content on spectral reflectance of bare soils in the 0.4–14  $\mu\text{m}$  domain. *International Journal of Remote Sensing*, 34(7):2268–2285, 2013.
- [27] Liu Weidong, Frédéric Baret, Gu Xingfa, Tong Qingxi, Zheng Lanfen, and Zhang Bing. Relating soil surface moisture to reflectance. *Remote Sensing of Environment*, 81(2-3):238–246, 2002.
- [28] David B Lobell and Gregory P Asner. Moisture effects on soil reflectance. *Soil Science Society of America Journal*, 66(3):722–727, 2002.
- [29] Jia Tian and William D Philpot. Relationship between surface soil water content, evaporation rate, and water absorption band depths in swir reflectance spectra. *Remote Sensing of Environment*, 169:280–289, 2015.

- [30] Jia Tian, Jibo Yue, William D Philpot, Xinyu Dong, and Qingjiu Tian. Soil moisture content estimate with drying process segmentation using shortwave infrared bands. *Remote Sensing of Environment*, 263:112552, 2021.
- [31] Brendan Malone, Uta Stockmann, Seija Tuomi, and Ben Sparrow. Tern surveillance monitoring program: Soil vis-nir spectral library with accompanying soil measurement data for 367 specimens. Data Collection, 2020.
- [32] Marcos AN Coutinho, Fernando de O Alari, Márcia MC Ferreira, and Lucas R do Amaral. Influence of soil sample preparation on the quantification of npk content via spectroscopy. *Geoderma*, 338:401–409, 2019.
- [33] Riikka Rinnan and Åsmund Rinnan. Application of near infrared reflectance (nir) and fluorescence spectroscopy to analysis of microbiological and chemical properties of arctic soil. *Soil Biology and Biochemistry*, 39(7):1664–1673, 2007.
- [34] S. Cipullo, S. Nawar, A. M. Mouazen, P. Campo-Moreno, and F. Coulon. Predicting bioavailability change of complex chemical mixtures in contaminated soils using visible and near-infrared spectroscopy and random forest regression. *Scientific Report*, 9(1):4492, 2019.
- [35] José AM Demattê, André Carneletto Dotto, Ariane FS Paiva, Marcus V Sato, Ricardo SD Dalmolin, B Maria do Socorro, Elisângela B da Silva, Marcos R Nanni, Alexandre ten Caten, Norberto C Noronha, et al. The brazilian soil spectral library (bssl): A general view, application and challenges. *Geoderma*, 354:113793, 2019.
- [36] Andrew Bissett and Raphael Viscarra Rossel. Soil visible–near infrared (vis–NIR) spectra for the Biomes of Australian Soil Environments (BASE) soil microbial diversity database, February 2022.
- [37] Bernard K Waruru, Keith D Shepherd, George M Ndegwa, Peter T Kamoni, and Andrew M Sila. Rapid estimation of soil engineering properties using diffuse reflectance near infrared spectroscopy. *Biosystems Engineering*, 121:177–185, 2014.
- [38] J. Sanderman, C. Smith, J. L. Safanelli, S. M. Mitu, Y. Ge, O. Murad, and K. Shepherd. Near-infrared (nir) soil spectral library using the neospectra handheld nir analyzer by si-ware, 2023.
- [39] JGB Leenaars, B Kempen, AJM van Oostrum, and NH Batjes. *Africa Soil Profiles Database: A compilation of georeferenced and standardised legacy soil profile data for Sub-Saharan Africa*, pages 51–57. 2014.
- [40] Pu Shi. Replication Data for: Vis-NIR spectroscopic assessment of soil aggregate stability and aggregate size distribution in the Belgian Loam Belt, 2020.
- [41] Tiago Rodrigues Tavares, José Paulo Molin, Elton Eduardo Novais Alves, Lidiane Cristina Nunes, Francisco José Krug, and Hudson Wallace Pereira de Carvalho. Spectral data of tropical

- soils using dry-chemistry techniques (vnir, xrf, and libs): a dataset for soil fertility prediction, 2022.
- [42] Jeanne Thoisy, Marie-Noel Mistou, Eric Latrille, Amandine Etayo, Virginie Rossard, Youssef Fouad, Cyril Girardin, and Fabien Gogé. French soil samples near infrared spectroscopy measurements and associated physico-chemical reference analysis., 2022.
- [43] Jeanne Thoisy, Marie-Noel Mistou, Amandine Etayo, Emmanuelle Vaudour, Eric Latrille, Virginie Rossard, and Cyril Girardin. Spectra transfer model of NIR spectra of soil samples., 2022.
- [44] D. Rizza, A. Rocci, and P. M. Chiarabaglio. Soil dataset from poplar cultivation sites in northern italy plains, 2023.
- [45] Mohammad R. Sadrian and Wendy M. Calvin. Spectral Measurements of Parent Soils from Globally Important Dust Aerosol Entrainment Regions, December 2022.
- [46] Felix Thomas, Marco Pohle, Ulrike Schmidt, and Ulrike Werban. Vis-NIRS spectral data and chemical properties of humus samples from forest soils in Saxony, 2020.
- [47] Bernard G. Barthès, Corinne Venkatapen, Aurélie Cambou, and Eric Blanchart. Data on soil organic carbon content and stock in Martinique – relations to near infrared spectra, 2023.
- [48] J. Hu, B. Murphy, and J. Huang. Soil texture, vis-nir spectra, and derived soil chemistry. UCAR/NCAR - Earth Observing Laboratory, 2020.
- [49] Ashish Vaswani, Noam Shazeer, Niki Parmar, Jakob Uszkoreit, Llion Jones, Aidan N Gomez, Lukasz Kaiser, and Illia Polosukhin. Attention is all you need. *Advances in Neural Information Processing Systems*, 30, 2017.
- [50] William H Press and Saul A Teukolsky. Savitzky-golay smoothing filters. *Computers in Physics*, 4(6):669–672, 1990.
- [51] Olaf Ronneberger, Philipp Fischer, and Thomas Brox. U-net: Convolutional networks for biomedical image segmentation. In *Medical Image Computing and Computer-Assisted Intervention–MICCAI 2015: 18th International Conference, Munich, Germany, October 5-9, 2015, Proceedings, Part III 18*, pages 234–241. Springer, 2015.
- [52] Tiankai Hang, Shuyang Gu, Chen Li, Jianmin Bao, Dong Chen, Han Hu, Xin Geng, and Baining Guo. Efficient diffusion training via min-snr weighting strategy. *arXiv preprint arXiv:2303.09556*, 2023.
- [53] Brian N. Bailey. A reverse ray-tracing method for modelling the net radiative flux in leaf-resolving plant canopy simulations. *Ecological Modelling*, 368:233–245, 2018.
- [54] J-L Widlowski, M Robustelli, M Disney, J-P Gastellu-Etchegorry, T Lavergne, P Lewis, PRJ North, B Pinty, R Thompson, and MM Verstraete. The RAMI On-line Model Checker (ROMC):

- A web-based benchmarking facility for canopy reflectance models. *Remote Sensing of Environment*, 112(3):1144–1150, 2008.
- [55] J-B Féret, AA Gitelson, SD Noble, and S Jacquemoud. PROSPECT-D: Towards modeling leaf optical properties through a complete lifecycle. *Remote Sensing of Environment*, 193:204–215, 2017.
- [56] Jean-Baptiste Féret, Katja Berger, Florian De Boissieu, and Zbyněk Malenovský. PROSPECT-PRO for estimating content of nitrogen-containing leaf proteins and other carbon-based constituents. *Remote Sensing of Environment*, 252:112173, 2021.
- [57] Dora Neina and Eunice Agyarko-Mintah. The terra preta model soil for sustainable sedentary yam production in west africa. *Heliyon*, 9(5), 2023.
- [58] Michael J Eden, Warwick Bray, Leonor Herrera, and Colin McEwan. Terra preta soils and their archaeological context in the caquetá basin of southeast colombia. *American Antiquity*, 49(1):125–140, 1984.
- [59] Stéphane Jacquemoud, Frédéric Baret, and JF Hanocq. Modeling spectral and bidirectional soil reflectance. *Remote Sensing of Environment*, 41(2-3):123–132, 1992.
- [60] Jianbo Qi, Donghui Xie, Tiangang Yin, Guangjian Yan, Jean-Philippe Gastellu-Etchegorry, Linyuan Li, Wuming Zhang, Xihan Mu, and Leslie K Norford. LESS: Large-Scale remote sensing data and image simulation framework over heterogeneous 3D scenes. *Remote Sensing of Environment*, 221:695–706, 2019.
- [61] Yingjie Wang and Jean-Philippe Gastellu-Etchegorry. Accurate and fast simulation of remote sensing images at top of atmosphere with DART-Lux. *Remote Sensing of Environment*, 256:112311, 2021.
- [62] Yingjie Wang, Abdelaziz Kallel, Xuebo Yang, Omar Regaieg, Nicolas Lauret, Jordan Guilleux, Eric Chavanon, and Jean-Philippe Gastellu-Etchegorry. DART-Lux: An unbiased and rapid Monte Carlo radiative transfer method for simulating remote sensing images. *Remote Sensing of Environment*, 274:112973, 2022.
- [63] Stéphane Jacquemoud and Frédéric Baret. PROSPECT: A model of leaf optical properties spectra. *Remote Sensing of Environment*, 34(2):75–91, 1990.
- [64] Jean-Baptiste Féret, Christophe François, Gregory P Asner, Anatoly A Gitelson, Roberta E Martin, Luc PR Bidel, Susan L Ustin, Gueric Le Maire, and Stéphane Jacquemoud. PROSPECT-4 and 5: Advances in the leaf optical properties model separating photosynthetic pigments. *Remote Sensing of Environment*, 112(6):3030–3043, 2008.
- [65] Wouter Verhoef. Light scattering by leaf layers with application to canopy reflectance modeling: The sail model. *Remote Sensing of Environment*, 16(2):125–141, 1984.

- [66] Wout Verhoef, Li Jia, Qing Xiao, and Zhongbo Su. Unified optical-thermal four-stream radiative transfer theory for homogeneous vegetation canopies. *IEEE Transactions on Geoscience and Remote Sensing*, 45(6):1808–1822, 2007.